communications

p-Type α-Fe₂O₃ Nanowires and their n-Type Transition in a Reductive Ambient**

Yu-Chen Lee, Yu-Lun Chueh, Chin-Hua Hsieh, Mu-Tung Chang, Li-Jen Chou,* Zhong Lin Wang, Yann-Wen Lan, Chii-Dong Chen, Hiroki Kurata, and Seiji Isoda

One-dimensional metal oxide nanomaterials have attracted much attention due to their semiconducting behavior and applications in nanodevices such as gas sensors, photo-diodes, field-effect transistors (FETs), and light-emitting diodes.[1] The control of electrons and holes, that is, n- or p-type nature, inside the functional metal oxide is of vital importance in the application of nanodevices. In general, n-type metal oxide nanomaterials are easily formed due to oxygen deficiencies (vacancies), which result in a donor level below but close to the conduction band. By contrast, p-type behavior is hard to achieve except in cases where the material is naturally p type. The common way to form the p type is through diffusion during the growth process or implantation into an as-grown sample, followed by post-annealing at high temperatures in order to eliminate defects.[2] By contrast, by using a reductive ambient, the direct transition between the n and p types of a metal oxide can be achieved through a change of dominant carriers on the surface, namely, those of electrons or holes. This n–p switch was first found in Cr_2O_3 under a treatment of ethanol vapor.[3] In addition, the n–p switch was found in other functional metal oxides, such as SnO_2, MoO_3, and In_2O_3, under certain kinds of reductive ambient.[4] However, the details of the n–p transition are still under investigation.

[*] Y.-C. Lee, Y.-L. Chueh, C.-H. Hsieh, M.-T. Chang, Prof. L.-J. Chou
Department of Materials Science and Engineering
National Tsing Hua University, Hsinchu, Taiwan 300 (ROC)
Fax: (+886) 35722366
E-mail: ljchou@mx.nthu.edu.tw

Y.-L. Chueh, Prof. Z. L. Wang
School of Materials Science and Engineering
Georgia Institute of Technology, Atlanta, GA 30332-0245 (USA)

Y.-W. Lan, Prof. C.-D. Chen
Institute of Physics
Academia Sinica, Nankang, 115, Taipei, Taiwan (ROC)

Prof. H. Kurata, Prof. S. Isoda
Institute for Chemical Research
Kyoto University, Uji, Kyoto 611-0011 (Japan)

Supporting information for this article is available on the WWW under http://www.small-journal.com or from the author.

α-Fe₂O₃ is the most stable iron oxide compound material and is widely used in photoelectrodes, gas sensing, catalysts, magnetic recording, and medical fields.[5] Recently, the n–p switch was demonstrated in an α-Fe₂O₃ thin-film sample after annealing with oxidation and reduction processes, for which the main principle was based on the surface adsorption of oxygen to increase band bending near the surface.[6] It is well known that the surface of a nanowire (NW) is very unstable, due to the large surface-to-volume ratio, and it easily adsorbs foreign molecules for stabilization.[7] By using NWs with unstable surface states, the n–p transition through surface adsorption is likely to be much more easily controlled and achieved than that with thick films. The divergence of measurement methods between our previous report[8] and Ref. [6] is consistent with our argument. Following our success in synthesizing α-Fe₂O₃ NWs with ordered oxygen vacancies,[8] in the present study we focus mainly on the electronic properties of those α-Fe₂O₃ NWs with oxygen vacancy orders in which the p-type nature can be found in as-grown NWs without any additional annealing. After a process of annealing in a reductive ambient, the p-type to n-type transition was observed. The detailed electronic structure of the α-Fe₂O₃ NWs before and after annealing was measured by electron energy loss spectrometry (EELS). The finding of a p–n transition suggests the potential application of the NWs in future nanodevices.

Figure 1a shows an SEM image of α-Fe₂O₃ NWs synthesized on an $Fe_{64}Ni_{36}$ substrate at 450°C for 10 h in an Ar ambient of 100 sccm. It is obvious that α-Fe₂O₃ NWs can be uniformly formed on a large scale. A typical TEM image of an α-Fe₂O₃ NW, with a diameter of ≈18 nm, is shown in Figure 1b. The sequential periodic structure with a regular spacing of 1.45 nm can be observed in the image shown in Figure 1c. The corresponding diffraction pattern, shown in Figure 1d, confirms the phase of α-Fe₂O₃ with a [001] zone axis. The extra spots can be found in the diffraction pattern after detailed examination and have ten times the distance of the $(3\bar{3}0)$ plane, as marked by arrows. Figure 1e shows the corresponding high-resolution TEM image highlighting the ordering structure. The two almost-identical d spacings of 0.25 nm are consistent with the d values of the $(2\bar{1}0)$ and (110) planes, thereby indicating the single-crystal nature of the wires with growth along the [110] direction. The long-range ordering phenomenon with a periodicity of 1.45 nm is located and marked by white arrows. The inset in the bottom of Figure 1e shows the corresponding fast Fourier transfer (FFT) of the image, which is accurately consistent with the results of the diffraction pattern. In order to clarify the ordering phenomenon found in both the diffraction pattern and the FFT pattern directly transformed from the high-resolution TEM image, the ideal high-resolution TEM image was processed by using an inverse FFT method through selection of only the matrix reflections from the stoichiometric α-Fe₂O₃ structure, as shown in Figure 1g. In a comparison of the three high-resolution images in Figure 1e–g, the ambiguous lattice image (dark image) between the two nearest bright dots can be seen (along the white arrows in Figure 1e); this is suggested to be caused by ordered oxygen vacancies. The atomic resolution image ac-
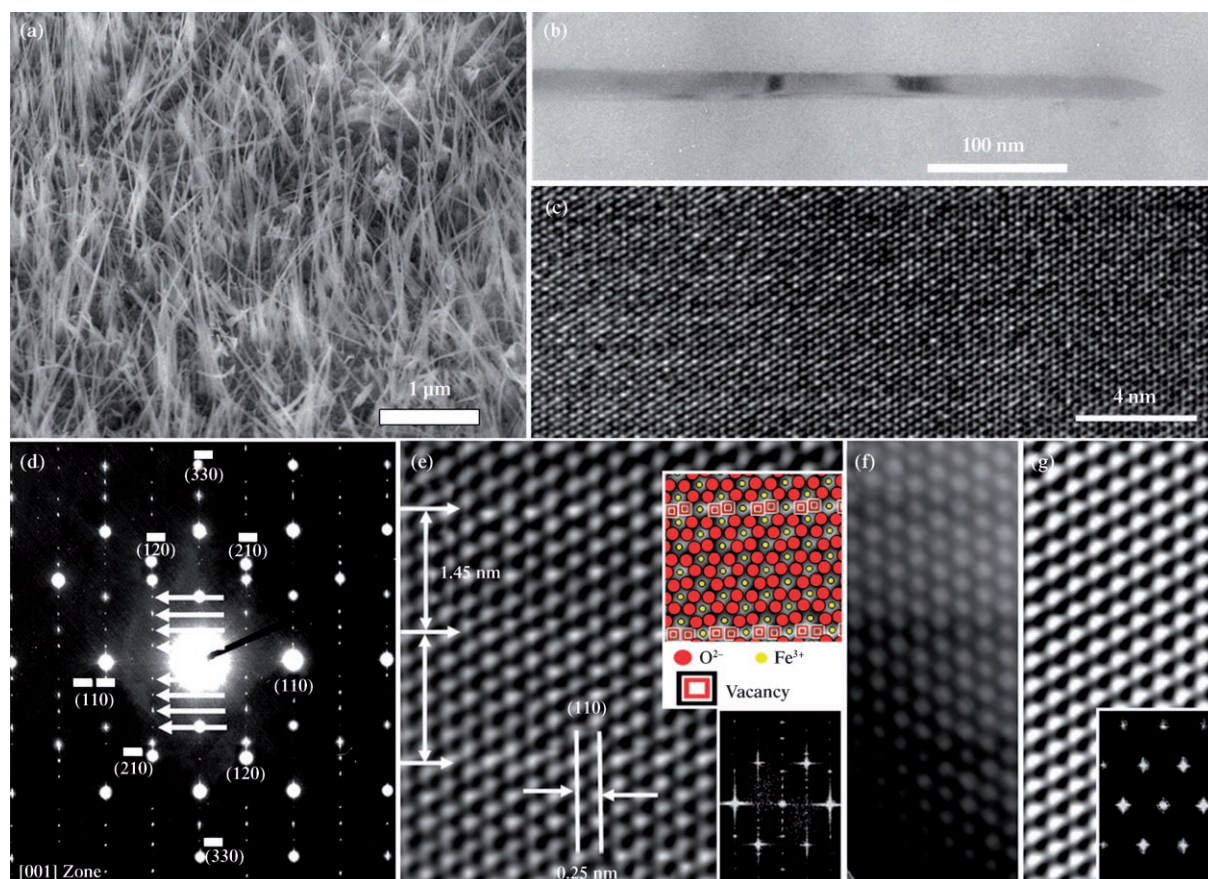
Figure 1. α-Fe$_2$O$_3$ NWs: a) A tilted SEM image. b) A low-magnification TEM image. c) A medium-magnification TEM image. d) The diffraction pattern with [001] zone axis as extracted from (c). The extra spots with ten times the distance of ($3\bar{3}0$)can be seen. e) A high-resolution TEM image recorded from (c). The regular lines can be distinctly observed. The hard-ball model (upper inset) is matched with the relative atomic position. The lower inset shows the fast Fourier transform (FFT) result, which is consistent with the diffraction pattern shown in (d). f) A high-resolution low-angle annular dark-field (LAADF) image. g) The Fourier filtered image made by removing the extra reflection spots. The inset shows the corresponding FFT image without the extra spots.

quired with scanning tunneling electron microscopy (STEM) by using an annular dark-field (ADF) detector, as shown in Figure 1 f, confirms the vacancy-ordering phenomenon owing to the presence of a strain field caused by oxygen deficiencies due to both the diffraction effect and weakened local scattering.[9] Furthermore, the hard-ball model, with removal of the oxygen atoms along the ten-period distance of the Fe–O lattice plane, fits coherently with the individual sites in the corresponding high-resolution TEM image, as shown in the upper inset of Figure 1e, where the yellow and red balls and the double rectangles represent the oxygen anions, iron cations, and oxygen vacancies caused by oxygen deficiency, respectively.

It is very interesting to note the influence on electrionc characteristics by high-order oxygen inside α-Fe$_2$O$_3$. Figure 2a shows the current as a function of the bias voltage under different gate voltages. The inset shows the two-terminal probe measurements for an α-Fe$_2$O$_3$ NW with a length and diameter of 0.12 μm and 37 nm, respectively. A resistance of 3.17 MΩ was found from the linear region, as the bias voltage went through zero voltage. However, this linear resistance does not exactly represent the entire resistance of the α-Fe$_2$O$_3$ NW due to the presence of contact re-

sistance between the NW and electrodes. With the increase of the gate voltage (-20 V to $+20$ V), an obvious decrease of channel conductance was found, which indicates that this α-Fe$_2$O$_3$ NW with high-order oxygen vacancies has a p-type semiconductor feature. In addition, a graph of the current as a function of the applied gate voltage (I/V_g curve shown in Figure 2b) gives us clear evidence of the p-type nature, since the current increased as the gate voltage decreased when a fixed voltage of 1 V was applied across the NW. For a typical cylindrical NW, the relationship of carrier density (cm^{-1}) and carrier mobility (cm^{2}V^{-1}s^{-1}) can be given by Equations (1) and (2).[10]

$$n = \frac{V_{gt}}{e} \times \frac{2\pi\varepsilon_0\varepsilon_r}{\ln(2h/r)} \qquad (1)$$

$$u = \frac{dI}{dV_g} \times \frac{\ln(2h/r)}{2\pi\varepsilon_0\varepsilon_r} \times \frac{L}{V_{ds}} \qquad (2)$$

V_{gt}, e, ε_r, h, and L, V_{ds} and r represent the threshold gate voltage, electron charge, relative dielectric constant ($\varepsilon_r = 3.9$ for SiO$_2$),[11] thickness of the gate oxide layer, channel
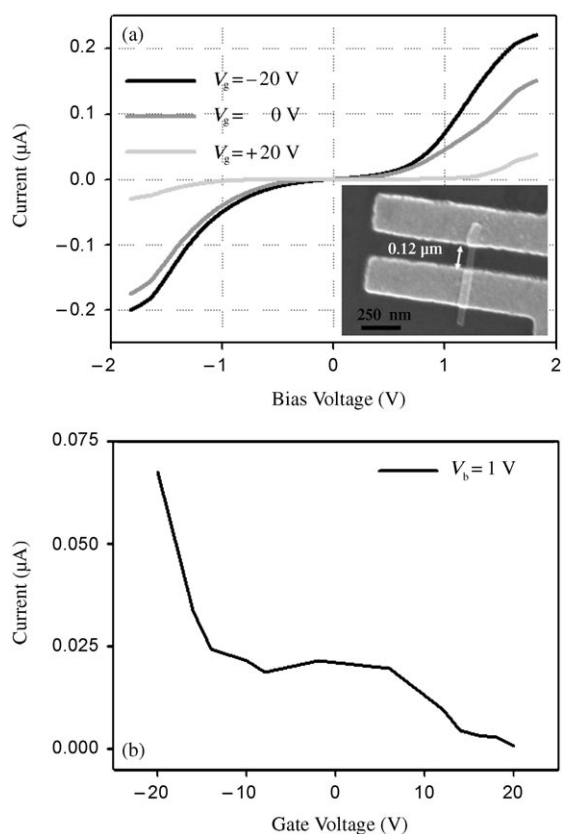
Figure 2. α-Fe₂O₃ NWs: a) Measurement of current versus bias voltage by applying different gate voltages ($V_g = +20$, 0, and -20 V). The inset shows the corresponding SEM image. b) Measurement of current versus different gate voltages at a bias voltage of $V_b = 1$ V.

length, bias voltage, and radius of the nanowire, respectively. The hole concentration and carrier mobility were found to be about 1.051×10^7 cm^{-1} and 4.22×10^{-2} cm^{2}V^{-1}s^{-1}, respectively, by extracting $V_{gt} = 2.3$ V and dI/d$V_g = 2.2 \times 10^{-9}$ AV^{-1} from Figure 2b; these values are consistent with the reported data.[12] Another device of the same α-Fe₂O₃ NW was prepared, and the I/V curve from this device, with different applied gate voltages, shows the same trend: the p-type semiconductor with a hole concentration and carrier mobility of 4.9×10^6 cm^{-1} and 3.09×10^{-2} cm^{2}V^{-1}s^{-1}, respectively (see Figure S1 in the Supporting Information).

In order to determine the specific p-type nature of the α-Fe₂O₃ NW, a chemical analysis on the electronic structure was imperative. In the present study, we focused on the EELS spectrum, which is sensitive to the electronic structure of the material. All raw EELS spectra were calibrated in the relative-energy position by a zero-loss peak and then subtracted by a power law to remove the background signal generated by plural scatting events. After recalibration of the energy position and removal of the multiscattering effect, the EELS measurements were deconvoluted by plasmons and a low-loss spectrum through a Fourier log to obtain the true single-scatting spectrum. Figure 3a shows the EELS spectrum of the oxygen k-edge energy loss near the edge fine structure (ELNES), taken from the center and edge regions of an α-Fe₂O₃ NW. The oxygen k-edge ELNES
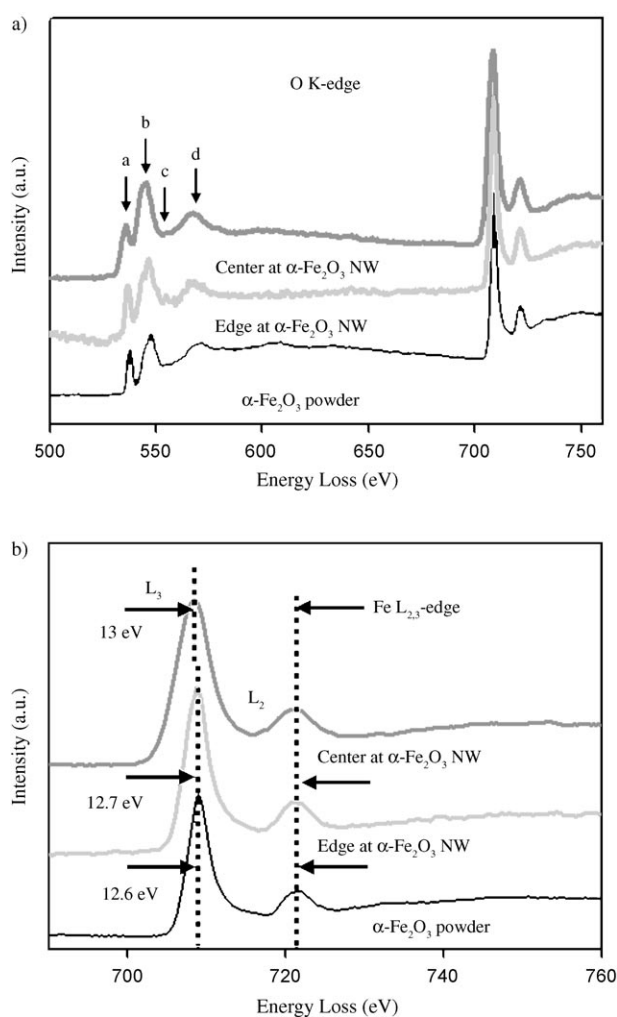

Figure 3. a) The EELS spectra of oxygen ELNES for α-Fe₂O₃ NWs at the center and edge regions and for the α-Fe₂O₃ powder. b) The corresponding EELS spectra of the L₂,₃ edge for α-Fe₂O₃ NWs at the center and edge regions and for the α-Fe₂O₃ powder.

spectrum from α-Fe₂O₃ powder is also shown at the bottom for comparison. Four peaks, labeled a–d, can be found in all of the spectra. In general, peak a is derived from the oxygen 1s to 2p core level hybridized with the iron 3d orbital, while peak b is derived from the oxygen 2p states hybridized with the transition-metal 4s and 4p states.[12] Peaks c and d result from the scattering of the third and first oxygen coordination shells by outgoing or backscattering electrons.[13,14]

In a comparison of the oxygen k-edge ELNES spectra acquired from the center and edge regions of the α-Fe₂O₃ NW, the relative intensity between the a and b peaks gradually becomes smaller. The decrease in intensity in peaks a and b is thought to be caused by oxygen vacancies inside the α-Fe₂O₃ NWs, which result in a diminishing hybridization of the metal 3d orbitals with the oxygen 2p orbitals.[13] In addition, the relative intensity between the a and b peaks at the edge regions of the α-Fe₂O₃ NWs is similar to that of the α-Fe₂O₃ powder, a result indicating that the oxygen deficiencies are compensated for by foreign molecules (oxygen and water molecules) through adsorption. However, the
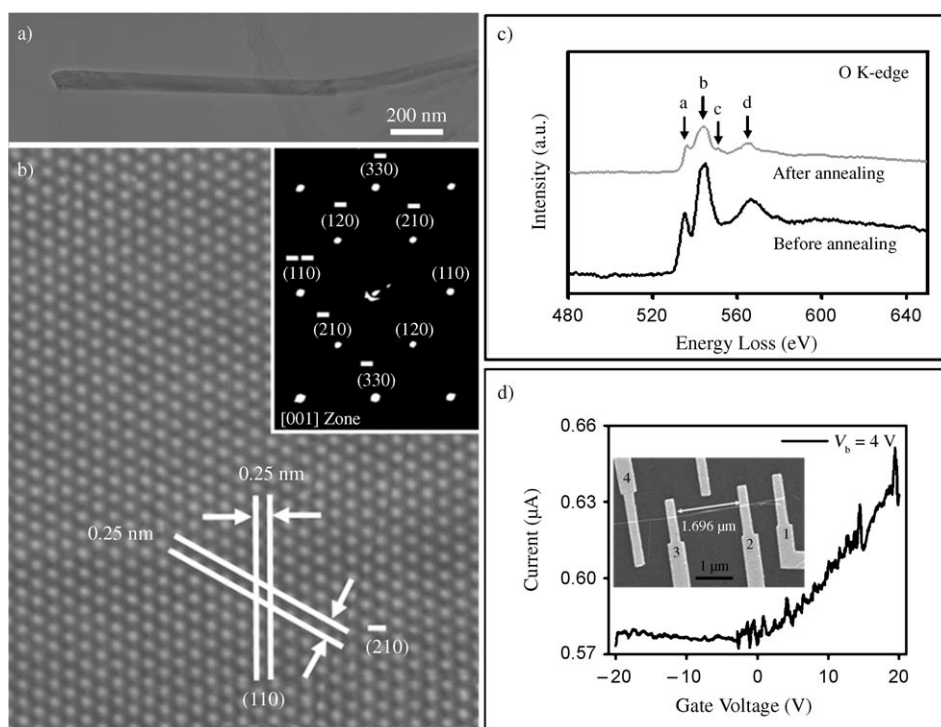
Figure 4. a) A low-magnification TEM image of an α-Fe$_2$O$_3$ NW after annealing in a reductive ambient. b) The corresponding high-resolution TEM image and diffraction pattern (inset). c) The EELS spectra of oxygen ELNES for α-Fe$_2$O$_3$ NWs before and after annealing in a reductive ambient. d) Measurement of current versus various gate voltages at $V_b = 4$. The inset shows the SEM image of the corresponding α-Fe$_2$O$_3$ nanodevices.

oxygen vacancy inside the α-Fe$_2$O$_3$ NWs can accompany a change in the oxidation states of the nearest neighbor Fe cations, which can be observed by EELS, as shown in Figure 3b, for which the EELS spectra of the iron L$_{2,3}$ edge are taken from the center and edge regions of the α-Fe$_2$O$_3$ NWs and from α-Fe$_2$O$_3$ powder, respectively. The L$_3$ and L$_2$ lines are the transitions of $2p^{3/2} \rightarrow 3d^{3/2}3d^{5/2}$ and $2p^{1/2} \rightarrow 3d^{3/2}$, respectively.[15] For the α-Fe$_2$O$_3$ powder, the difference between the relative positions of L$_3$ and L$_2$ is found to be about 12.6 eV, while for α-Fe$_2$O$_3$ NWs the differences between the relative positions of L$_3$ and L$_2$ at the edge and center regions are found about ≈12.7 and 13 eV, respectively. The energy difference of 0.4 eV obtained from the relative positions of the L$_3$ and L$_2$ lines in the center region of the α-Fe$_2$O$_3$ NWs and in the powder most likely results from the oxygen vacancies, which partially decrease the oxidation states of the Fe cations from Fe^{3+} to Fe^{2+}.[13] However, for the edge region of the α-Fe$_2$O$_3$ NWs and the powder, no obvious energy shift can be found, a result indicating that the oxidation states of the Fe cations should be the same as the bulk counterpart.

After an annealing process at 450 °C in a reductive ambient, the morphology did not change, as shown in Figure 4a. In addition, the high-resolution TEM image and the corresponding diffraction shown in Figure 4b, in which the individual planes in the diffraction pattern with a [001] zone axis and two *d* spacings in the high-resolution TEM image were indexed and illustrated, confirmed no oxygen vacancy

ordering. Therefore, annealing in a reductive ambient not only limited the oxygen molecules adsorbing on the surface but also created more oxygen vacancies inside the α-Fe$_2$O$_3$ through removal of oxygen anions from the α-Fe$_2$O$_3$ lattice.[16] During the reduction process, more oxygen anions diffused to the surface, thereby resulting in the creation of oxygen vacancies. Thus, this diffusion behavior may likely destroy the oxygen vacancy ordering inside the α-Fe$_2$O$_3$ NW. From the EELS spectra of the oxygen k-edge ELNES for the α-Fe$_2$O$_3$ NWs before and after the annealing in a reductive ambient, as shown in Figure 4c, the significant change in the a:b ratio after the annealing process in a reductive ambient clearly proves that the density of oxygen vacancies was increased, which is consistent with previous reports.[8,17] Figure 4d describes the *I–V* characteristics as a function of different gate voltages (from −20 to +20 V) for a α-Fe$_2$O$_3$ NW with a length and diameter of 1.7 μm and 32 nm, respectively, after annealing in a reductive ambient; the corresponding device is shown in the inset image. Surprisingly, the conductance was increased as the forward gate voltage was increased, a result indicating the n-type nature. Accordingly, from Equations (1) and (2), the electron concentration and mobility were found to be 1.452×10^7 cm^{-1} and 1.574×10^{-3} cm^2 V^{-1} s^{-1} by taking $V_{gt} = -3.45$ V and $dI/dV = 25 \times 10^{-12}$ A V^{-1}, as extrapolated from the linear region (+4 to +20 V) of the I/V_g curve; these results nearly match the previous data.[12]

In general, the oxygen deficiencies inside the metal oxide nanomaterials should result in an n-type nature, and the corresponding band diagram is schematically drawn in Figure 5a, where the Fermi level (E_F) is above the intrinsic Fermi level (E_i). Due to the larger density of the unstable surface state, the adsorption of oxygen and water molecules on the surface of metal oxide NWs can cause bending and a change in work function, which results in the formation of a depletion layer and a decrease in the conductance near the surface.[18] However, NWs with wide-bandgap features still retain an n-type conductivity, for example, ZnO NWs (3.4 eV), SnO$_2$ NWs (3.6 eV), and TiO$_2$ NWs (3.2 eV). It is well known that its narrow bandgap of 2.2 eV makes α-Fe$_2$O$_3$ a typical n-type semiconductor at low synthesis temperatures with pure oxide stoichiometry, but it then becomes a p-type semiconductor at high synthesis tempera-
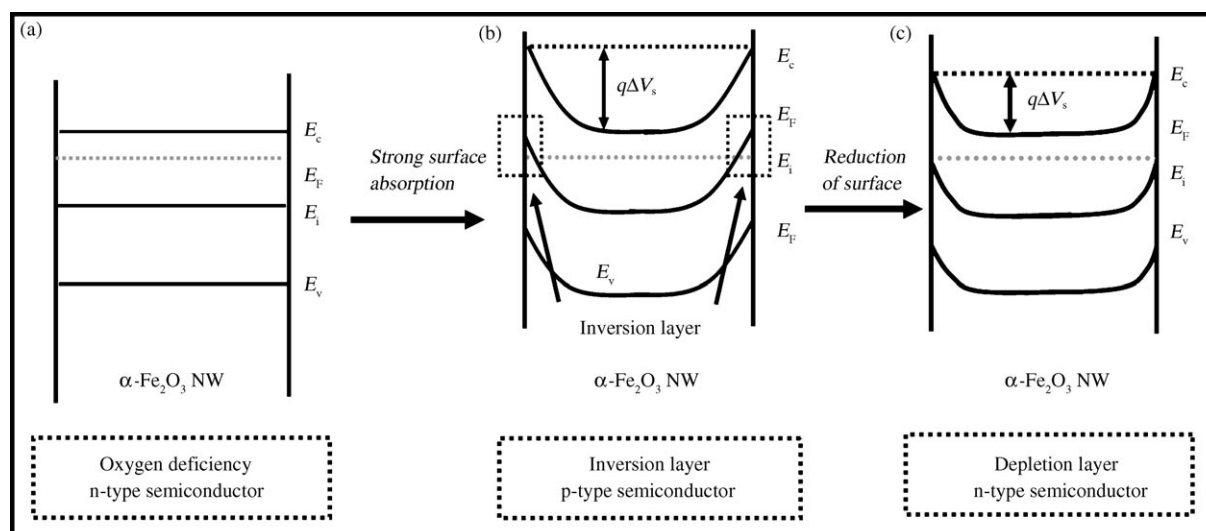
Figure 5. Schematic energy-level diagrams of a) an n-type semiconductor caused by oxygen vacancies, b) a p-type semiconductor through formation of an inversion layer caused by strong surface absorption owing to the oxygen vacancy order, and c) the depletion layer caused by surface absorption.

tures with impure oxide stoichiometry.[16a,19] The previous reports demonstrate the n-type nature of α-Fe$_2$O$_3$ NWs due to surface adsorption, which causes a depletion layer on the surface, but the major carriers were still electrons, which indicates the n-type feature.[12b] By contrast, our results show the opposite tendency, namely, a p-type nature for as-grown samples. Based on the EELS results for the center and edge regions of α-Fe$_2$O$_3$, we theorize that the p-type tendency can be considered to result from the formation of an inversion layer, which originates from the strong surface absorption of oxygen and water molecules near the surface due to the large density of unstable surface states because of the oxygen vacancy ordering, as shown in Figure 5b. After annealing in a reductive ambient, the switch from p- to n-type can be clearly seen in the I/V_g characteristics. During the reductive process, the removal of oxygen anions from the α-Fe$_2$O$_3$ lattice could result in an increase of oxygen vacancies to destroy the balance of the oxygen vacancy order. Although the density of oxygen vacancies was high, the surface adsorption caused a depletion layer instead of an inversion layer, as shown in Figure 5c, which was in reasonable agreement with the experimental results. In addition, the increase in oxygen vacancies resulted in deviation from the stoichiometry, that is, α-Fe$_2$O$_{3-x}$, where x is proportional to the density of oxygen vacancies, and thus led to a lower oxide compound, namely magnetite (Fe$_3$O$_4$), after consecutive annealing processes at high temperatures and long annealing times.[20] Determination of the p-type nature of α-Fe$_2$O$_3$ for as-grown samples and then conversion to n-type nature by simply annealing at lower temperatures in a reductive ambient facilitates promising and various applications in nanodevices.

In conclusion, the p-type conductivity of α-Fe$_2$O$_3$ with the oxygen vacancy order was found without any treatment. The detailed characteristics of the p-type nature were mainly caused by strong surface adsorption owing to the oxygen vacancies and the large surface-to-volume ratio. This

strong surface adsorption was confirmed by EELS. After an annealing process at 450 °C in a reductive ambient, a disappearance of oxygen vacancy ordering and an increase of oxygen vacancy density was found by EELS analysis. From the I/V curve, the NW then exhibited an n-type nature. The p–n switch promises potential applications for NWs in nanodevices.

Experimental Section

Iron-based substrates of 1.5 cm^2 were used to grow the α-Fe$_2$O$_3$ NWs. The furnace was of a typical three-zone tube type, consisting of a vacuum pumping system, an alumina tube, a quartz tube, and a gas-flow system (from Zimberger Inc). The ultimate vacuum level for this configuration was 3×10^{-2} Torr and the maximum output temperature could reach ≈ 1500 °C. The quartz tube was inset into the alumina tube in order to avoid contamination of the outside alumina tube during the synthesis of the NWs. The system was pumped to the base pressure of 3×10^{-2} Torr and then maintained at a pressure of 500–1000 mbar by the introduction of Ar carrier gas (99.995 %) at a flow rate of 70–150 sccm, controlled by a mass-flow controller (MFC). The iron-based substrates were put into the lower temperature region at 350–700 °C for 10 h, and an α-Fe$_2$O$_3$ commercial powder (5 g) was placed in the high-temperature region at 1200 °C. The ramping rate was kept at 5 °C min^{-1} at the desired temperature, and the system was allowed to cool down naturally to room temperature. The detailed growth parameters are depicted elsewhere.[8]

For the reduction process, the NWs were annealed in a mixed reductive ambient of H$_2$ (5 %) + Ar (95 %) at a temperature of 450 °C for 10–20 min in the furnace. The surface morphology was examined by a field-emission scanning electron microscope (JSM-6500F) operated at 15 kV. In order to prepare the TEM specimen, all of the samples were sonicated in ethanol before being dispersed on a copper grid supported by a holey

carbon film. A field-emission transmission electron microscope (JEM-3000F) operating at 300 kV, with a point-to-point resolution of 0.17 nm and equipped with an energy dispersion X-ray spectrometer (EDS) and an electron energy loss spectrometer (EELS), was used to measure the microstructures and chemical compositions. For the electronic measurements, the α-Fe_2O_3 NWs were transferred onto 0.7×0.7 cm^2 chips with well-defined Au lead patterns on a Si substrate with a 300-nm-thick thermal oxide layer. Ni (35 nm)/Au (65 nm) leads were measured by a thermal field-emission scanning electron microscope (FEI Sirion) and deposited by a homemade two-boat thermal evaporator. After the electrode deposition, a lift-off process was carried out to strip off the resist to obtain the designed electrode pattern on the chip surface. The I/V measurement equipment, including multimeters, voltage sources, oscilloscope, lock-in amplifiers, power supply, and AC bridge for the temperature controller were controlled by a LabView program. Different gate voltages (from -20 V to $+20$ V) were applied to determine the field-effect characteristics. The $I–V$ characteristics of α-Fe_2O_3 are available in the Supporting Information.

Keywords:

[1] a) T. H. Moon, M. C. Jeong, B. Y. Oh, M. H. Ham, M. H. Jeun, W. Y. Lee, J. M. Myoung, *Nanotechnology* **2006**, *17*, 2116; b) Z. L. Wang, J. H. Song, *Science* **2006**, *312*, 242; c) P. Nguyen, H. T. Ng, T. Yamada, M. K. Smith, J. Li, J. Han, M. Meyyappan, *Nano Lett.* **2004**, *4*, 651; d) Y. R. Ryu, T. S. Lee, J. A. Lubguban, H. W. White, Y. S. Park, C. J. Youn, *Appl. Phys. Lett.* **2005**, *87*, 153504; e) C. S. Lao, P. X. Gao, L. Zhang, D. Davidovic, R. Tummala, Z. L. Wang, *Nano Lett.* **2006**, *6*, 263; f) A. Ponzoni, E. Comini, G. Sberveglieri, J. Zhou, S. Z. Deng, N. S. Xu, Y. Ding, Z. L. Wang, *Appl. Phys. Lett.* **2006**, *88*, 203106.

[2] C. Ronning, P. X. Gao, Z. L. Wang, D. Schwen, *Appl. Phys. Lett.* **2004**, *84*, 783.

[3] A. Bielanski, J. Deren, J. Haber, *Nature* **1957**, *179*, 668.

[4] a) B. W. Licznerski, K. Nitsch, H. Teterycz, K. Wisniewski, *Sens. Actuators B* **1992**, *7*, 626; b) A. K. Prasad, D. J. Kubinski, P. I.

Gouma, *Sens. Actuators B* **2003**, *93*, 25; c) G. Korotcenkov, V. Brinzari, V. Golovanov, A. Cerneavshi, V. Matolin, A. Todd, *Appl. Surf. Sci.* **2004**, *227*, 122.

[5] a) M. Catti, G. Valerio, *Phys. Rev. B* **1995**, *51*, 7441; b) J. Chen, L. Xu, W. Li, X. Gou, *Adv. Mater.* **2005**, *17*, 582.

[6] A. Gurlo, N. Bârsan, A. Oprea, M. Sahm, T. Sahm, U. Weimar, *Appl. Phys. Lett.* **2004**, *85*, 2280.

[7] a) S. Mathur, S. Barth, H. Shen, J. C. Pyun, U. Werner, *Small* **2005**, *1*, 713; b) Q. H. Li, T. Gao, Y. G. Wang, T. H. Wang, *Appl. Phys. Lett.* **2005**, *86*, 123117; c) H. Kind, H. Yan, B. Messer, M. Law, P. D. Yang, *Adv. Mater.* **2002**, *14*, 158.

[8] Y. L. Chueh, M. W. Lai, J. Q. Liang, L. J. Chou, Z. L. Wang, *Adv. Funct. Mater.* **2006**, *16*, 2243.

[9] Z. Yu, D. A. Muller, J. Silcox, *J. Appl. Phys.* **2004**, *95*, 3362.

[10] a) J. E. Fischer, H. Dai, A. Thess, R. Lee, N. M. Hanjani, D. L. Dehaas, R. E. Smalley, *Phys. Rev. B* **1997**, *55*, 4921; b) R. Martel, T. Schmidt, H. R. Shea, T. Hertel, P. Avouris, *Appl. Phys. Lett.* **1998**, *73*, 2447; c) Z. Fan, D. Wang, P. C. Chang, W. Y. Tseng, J. G. Lu, *Appl. Phys. Lett.* **2004**, *85*, 5923.

[11] S. M. Sze, *Modern Semiconductor Device Physics*, Wiley, New York, **1998**.

[12] a) F. J. Morin, *Phys. Rev.* **1954**, *93*, 1195; b) Z. Fan, X. Wen, S. Yang, J. G. Lu, *Appl. Phys. Lett.* **2005**, *87*, 013113.

[13] C. Colliex, T. Manoubi, C. Ortiz, *Phys. Rev. B* **1991**, *44*, 11402.

[14] H. Kurata, E. Lefèvre, C. Colliex, R. Brydson, *Phys. Rev. B* **1993**, *47*, 13763.

[15] Z. L. Wang, J. S. Yin, Y. D. Jiang, J. Zhang, *Appl. Phys. Lett.* **1997**, *70*, 3362.

[16] a) D. J. M. Bevan, J. P. Shelton, J. S. Anderson, *J. Chem. Soc.* **1948**, 1729; b) R. F. G. Gardner, F. Sweetand, D. W. Tanner, *J. Phys. Chem. Solids* **1963**, *24*, 1193.

[17] J. Jasinski, K. E. Pinkerton, I. M. Kennedy, V. J. Leppert, *Sens. Actuators B* **2005**, *109*, 19.

[18] S. R. Morrison, *The Chemical Physics of Surfaces*, Plenum, New York, **1990**.

[19] K. Kobayash, G. Okada, J. Kumanotani, *J. Mater. Sci. Lett.* **1988**, *7*, 853.

[20] a) M. H. A. Elhamid, M. M. Khader, A. E. Mahgoub, B. E. E. Anadouli, B. G. Ateya, *J. Solid State Chem.* **1996**, *123*, 249; b) P. K. Gallagher, E. M. Gyorgy, H. E. Bair, *J. Chem. Phys.* **1979**, *71*, 830.